PSFC/JA-04-61

Role of trapped electron mode turbulence in internal transport barrier control in the Alcator C-Mod Tokamak

Ernst, D. R.; Bonoli, P. T.; Catto, P. J.; Dorland, W.*; Fiore, C. L.;Granetz, R. S.; Greenwald, M.; Hubbard, A. E.; Porkolab, M.; Redi, M. H.**; Rice, J. E.; Zhurovich, K.; and the Alcator C-Mod Group

* University of Maryland
** Princeton Plasma Physics Laboratory

Plasma Science and Fusion Center
Massachusetts Institute of Technology
Cambridge MA 02139 USA

This work was supported by the U.S. Department of Energy, Grant No. DE-FC02-99ER54512.

Role of trapped electron mode turbulence in internal transport barrier control in the Alcator C-Mod Tokamak*

D. R. Ernst,† P. T. Bonoli, P. J. Catto, W. Dorland,‡ C. L. Fiore, R. S. Granetz, M. Greenwald, A. E. Hubbard, M. Porkolab, M. H. Redi,§ J. E. Rice, K. Zhurovich, and the Alcator C-Mod Group

Plasma Science and Fusion Center
Massachusetts Institute of Technology
167 Albany Street, NW16-258
Cambridge, Massachusetts 02139

Nonlinear gyrokinetic simulations of trapped electron mode (TEM) turbulence, within an internal particle transport barrier, are performed and compared with experimental data. The results provide a mechanism for transport barrier control with on-axis radio frequency heating, as demonstrated in Alcator C-Mod experiments [S. J. Wukitch *et al.*, Phys. Plasmas **9**(5) 2149 (2002)]. Off-axis heating produces an internal particle and energy transport barrier after the transition to enhanced Dα high confinement mode. The barrier foot reaches the half-radius, with a peak density 2.5 times the edge density. While the density profile peaks, the temperature profile remains relatively unaffected. The peaking and concomitant impurity accumulation are controlled by applying modest central heating power late in the discharge. Gyrokinetic turbulence simulations of the barrier formation phase, using the GS2 code [W. Dorland *et al.*, Phys. Rev. Lett. 85, 5579 (2000)] show that toroidal ion temperature gradient driven modes are suppressed inside the barrier foot, but continue to dominate in the outer half-radius. As the density gradient steepens further, trapped electron modes are driven unstable. The onset of TEM turbulence produces an outflow that strongly increases with the density gradient, upon exceeding a new nonlinear critical density gradient, which significantly exceeds the linear critical density gradient. The TEM turbulent outflow ultimately balances the inward Ware pinch, leading to steady state. Moreover, the simulated turbulent particle diffusivity matches that inferred from particle balance using measured density profile data and the calculated Ware pinch. This turbulent diffusivity exhibits a strong unfavorable temperature dependence that allows control with central heating.

PACS numbers: 52.25.Fi,52.25.Vy,52.30.Gz,52.35.Kt,52.35.Ra,52.50.Qt,52.55.Dy,52.55.Fa,52.65.Tt

I. INTRODUCTION

Significant progress was made over the last decade toward quantitative, fundamental calculations of turbulent ion thermal transport [1] resulting from toroidal ion temperature gradient driven modes [2]. The work presented in this paper focuses on particle and electron thermal transport, which are relatively unexplored, particularly in internal transport barriers. In the experiments analyzed, trapped electron modes (TEM) are clearly dominant, there is no particle source, and the temperature gradient plays little role. In an effort to understand basic particle transport processes underlying spontaneous formation and subsequent control of the internal particle and energy transport barriers in Alcator C-Mod tokamak, we simulate trapped electron mode turbulence using the nonlinear gyrokinetic turbulence code GS2 [3, 4]. The simulations are carried out using input data preparation and plotting tools first described in Ref. [5]. The work presented provides a mechanism for the demonstrated density and impurity profile control with on-axis ion cyclotron heating in Alcator C-Mod experiments [6, 7]. Several new results on trapped electron mode stability and transport are uncovered as well. After investigating the relevant linear stability properties of the TEM, we find in nonlinear simulations that no turbulent transport is produced until the linear critical density gradient is exceeded by a significant margin. Analogous to the Dimits shift [1] of the nonlinear critical temperature gradient for toroidal ITG modes, this upshift of the TEM critical density gradient results from suppression by turbulence-generated zonal flows.

The fusion power produced in a tokamak reactor scales with the square of the plasma pressure, which is limited by plasma confinement. Our present understanding of ion thermal transport in tokamak plasmas [1, 8–10] suggests that toroidal ion temperature gradient (ITG) driven turbulence [2] plays a central role in determining the core ion temperature profile. Because the ion thermal transport produced by toroidal ITG driven turbulence increases very strongly with the temperature gradient after the critical gradient is exceeded, the linear stability properties are a strong influence. When toroidal ITG modes are unstable, the ion temperature gradient must deviate only slightly from the critical gradient for the turbu-

*Paper UI1 5, Bull. Am. Phys. Soc. **48**, 332 (2003); *Physics of Plasmas*, **11**(5) 2637 (2004).
†Electronic address: dernst@psfc.mit.edu
‡Department of Physics, Univ. of Maryland, 3325 A.V. Williams Building, College Park, Maryland 20742
§Princeton Plasma Physics Laboratory, P. O. Box 451, Princeton, New Jersey, 08543

lent diffusion to transport the integrated heating power. Trapped electron modes have thus far been considered a minor perturbation to this overall picture, and turbulent particle transport has been little studied.

Internal transport barriers offer potential relief from the stability constraint imposed by toroidal ITG modes, demonstrating self-organization of the core to a state of higher pressure. Internal transport barriers (ITBs) can be reliably initiated in many regimes, most often with neutral beam injection heating in the presence of fast current ramping. Double transport barrier modes characterized by an internal transport barrier and an H-mode edge have also been reported in the ASDEX Upgrade device [11], JT60-U [12], JET [13], and in the DIII-D tokamak [14], as well as in Alcator C-Mod experiments[6, 15]. However, internal transport barriers are often reliant upon reversed magnetic shear, strong radial electric field shear, large Shafranov shift, hot ions, or impurity content. It is generally known that many of these conditions scale unfavorably with plasma size or are otherwise undesireable in a reactor [16]. The International Tokamak Experimental Reactor (ITER) [17], for example, is envisioned to operate mainly in the Edge Localized Mode High-Mode (ELMy H-Mode) regime, which is characterized by a relatively flat density profile, a moderately peaked temperature profile, and monotonic safety factor profile, with comparable ion and electron temperatures. The C-Mod experiments have achieved double transport barriers without relying on reversed magnetic shear, large Shafranov shift, impurity content, hot ions, or externally driven toroidal rotation. Advanced scenarios with internal transport barriers are under investigation for ITER.

The empirical scaling for the thermal confinement time in the ELMy H-Mode regime shows an unfavorable degradation with heating power with an exponent of -0.6 [17, 18]. On the other hand, many improved confinement regimes, particularly those with internal transport barriers, display favorable scaling of core confinement with heating power, arising in part from reduction of turbulent transport due to radial electric field shear [10]. The C-Mod experiments display the opposite behavior with respect to on-axis heating inside the ITB, which has proven to be beneficial as a means of control when the on-axis power is less than 0.8 MW.

Internal transport barriers have been observed to form in Alcator C-Mod [19] in the presence of intense off-axis minority ion-cyclotron resonance heating [6, 15, 20] during H-mode back-transitions [20], and in plasmas with pure ohmic heating [15, 20]. Figure 1 shows the temporal evolution of the Alcator C-Mod case we consider. Here the ITB was produced with 2 MW of 80 MHz off-axis minority ICRH and the density rise was arrested starting at 1.25 seconds with 0.6 MW of on-axis ICRH. This example of transport barrier control with on-axis heating has been extended to the case of ITBs produced with ohmic heating alone [21].

Few investigations of particle transport, within transport barriers, have been carried out. Work on Tokamak Fusion Test Reactor reverse shear plasmas [22], found transport close to neoclassical where turbulent transport was suppressed. A recent study of impurity transport in Doublet-III-D (DIII-D) Quiescent Double Barrier plasmas found impurity transport greatly exceeding neoclassical [23]. Simulations of Joint European Torus (JET) ITB plasmas using GS2 found simulated turbulent transport greatly exceeding measured [24]. In this paper, we find quantitative agreement, within uncertainties, between gyrokinetic turbulence simulations and measured particle and energy transport, within an internal transport barrier, without adjustable parameters.

II. OVERVIEW OF EXPERIMENTS

The Alcator C-Mod tokamak is a compact, high field machine with major radius 67 cm, minor radius 21 cm (typ.), elongation up to 1.8, toroidal magnetic field between 2.7 and 8.0 T, and plasma currents from 0.23 to 1.7 MA in the lower single null configuration. In the experiments considered here [6], the on-axis toroidal field was 4.5 T with plasma current 0.8 MA. The temporal evolution of the C-Mod ITB discharge we consider is shown in Fig. 1. Shortly after 2 MW off-axis hydrogen minority ion cyclotron frequency resonant heating (ICRH) at 80 MHz is applied to the high field side, at 0.7 seconds, the transition to EDA H-Mode occurs, as shown in the visible bremsstrahlung (VB) emission profiles of Fig. 2. The ion cyclotron heating power density peaks near the half-radius, which is very near the ITB foot location in this case. The core density inside the heating radius begins to rise immediately following the H-mode transition and steadily continues to rise until arrested by 0.6 MW of on-axis 70 MHz hydrogen minority ICRH at 1.25 seconds. The core $Z_{\rm eff}$ rises from values close to unity in the early H-Mode phase to a maximum of 1.8 during on-axis heating. This external control of particle transport within an ITB, using radio frequency heating, prevents radiative collapse due to accumulation of impurities inside the ITB. Such profile control would have great utility if made possible in a reactor, not only preventing impurity accumulation that plagues most ITBs, but also helping to avoid the MHD ballooning stability limit [25, 26]. Further Alcator C-Mod experiments have shown that the central density can be adjusted by controlling the on-axis ICRH power and timing of its onset [7, 21], with powers exceeding 0.9-1.0 MW resulting in a flattening of the density profile.

Recently, Thomson scattering measurements on C-Mod have doubled their radial resolution, although the laser interval remains of order the energy confinement time. Recent calibrations for the density measurement utilize the density at which second harmonic electron cyclotron emission is cut off. We have written a profile fitting code for Thomson scattering density profiles in ITBs. The code improves the effective radial resolution of the Thomson scattering density profile by constrain-

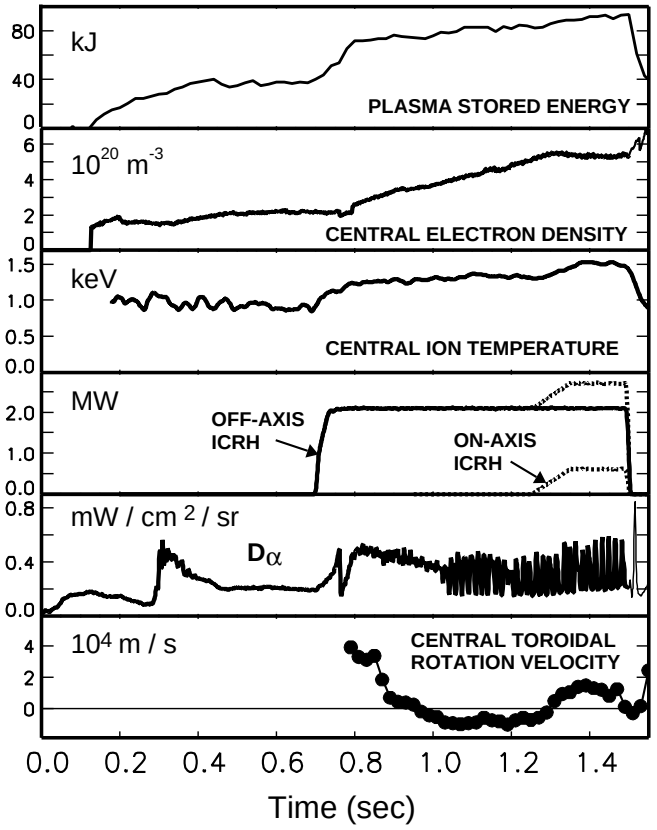

FIG. 1: Temporal evolution of C-Mod ITB discharge. Off-axis ICRH (2.0 MW) begins at 0.7 seconds, initiating a transition to EDA H-Mode, as shown by the Dα emission. As the central density ($n_e\sqrt{Z_{\rm eff}}$) steadily rises, the ion and electron temperatures do not degrade, indicating improving energy confinement. As the ITB forms, the central toroidal rotation velocity suddenly changes sign from the co- to counter-current direction. At 1.25 seconds, 0.6 MW of on-axis ICRH is applied, arresting the density rise.

ing the ITB foot location, as found from VB emission profiles with ∼1 mm channel spacing. Some initial results of this fitting procedure are shown in Ref. [21]. The $Z_{\rm eff}$ profiles are obtained by combining Thomson scattering density profiles with calibrated VB measurements of $n_e\sqrt{Z_{\rm eff}}$. The resulting $Z_{\rm eff}$ profile is flat outside the ITB foot, and peaks off-axis. These more recent data allow us to estimate error bars on the density gradient scale length we obtained from VB emission profiles alone, assuming flat $Z_{\rm eff}$.

The temperature profiles in this study were measured by X-ray spectroscopy (HIREX) [7], with a point on-axis inferred from TRANSP analysis by matching the measured neutron rate. The electron temperature was taken equal to the ion temperature. However, more recent experiments [21] have utilized larger magnetic fields, with off-axis heating on the outboard side, to avoid high-density cutoff of the electron cyclotron emission (ECE). For these cases, full ECE electron temperature profiles are available, which in some cases, show a slight break in slope at the ITB radius. The quality of this newer data may allow us to draw more detailed conclusions in the future regarding stability to toroidal ion temperature gradient (ITG) modes during the initial barrier formation phase. As shown in the following, the shape of the temperature profile is unimportant in the later phase of the discharge.

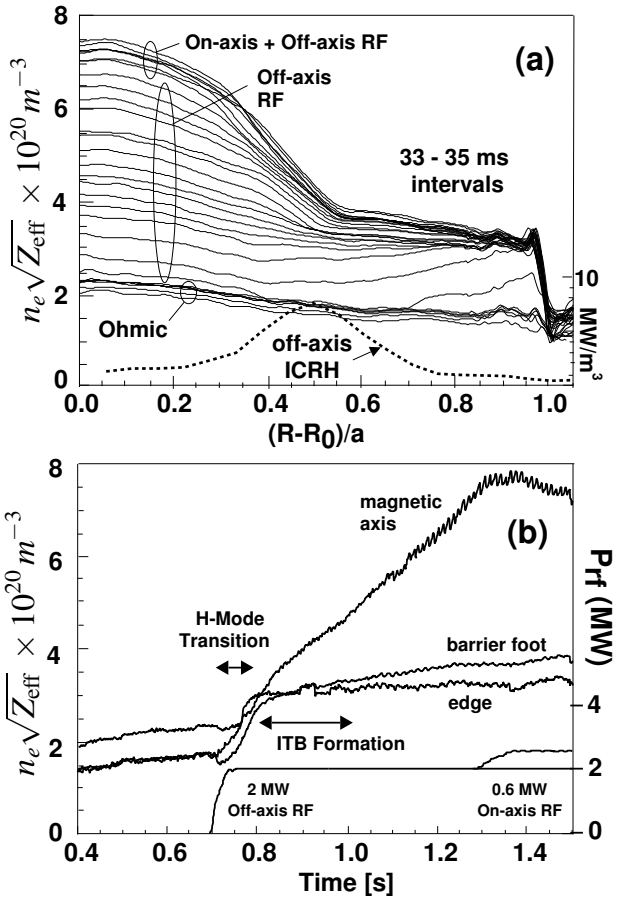

FIG. 2: (a) Density profiles measured by 218 channel visible bremsstrahlung emission spectroscopy at regular intervals, with approximately 1 mm channel spacing. (b) Density at the magnetic axis, ITB foot, and just inside the H-Mode edge pedestal as a function of time, together with the ICRH power.

The C-Mod experiments are characterized by very high core densities $\sim 6\times10^{20}\,m^{-3}$, yet there is no central fueling. There is no apparent external momentum input, but the toroidal rotation is anomalous in the co-direction and displays interesting dynamics with ITB formation [7], changing direction from co- to counter-current. The safety factor radial profile (q) is monotonic from equilibrium reconstruction (EFIT [27] and TRANSP [28]). Motional Stark Effect (MSE) measurements of q are under development. The Shafranov shift is very small, eliminating another stabilizing factor which plays a significant role in many other internal transport barriers [14, 25, 26, 29]. Radial electric field shear [10, 30] ap-

pears to be unimportant after ITB formation, further eliminating ambiguity in our comparisons. Because there are no particle sources or sinks in the plasma core, the continuity equation takes a particularly simple form,

$$\frac{\partial n_e}{\partial t} + \nabla \cdot (\Gamma_{\rm Ware} - D_{\rm eff} \nabla n_e) = 0. \qquad (1)$$

Figure 3 shows the result of inverting this equation to obtain the effective diffusivity, from the measured VB density profiles together with the Ware pinch, $\Gamma_{\rm Ware}$, calculated from Ref. [31]. The Ware pinch calculated analytically from the moments approach [32] (as in TRANSP) gives nearly identical results. The toroidal electric field was obtained from the TRANSP solution to the poloidal magnetic field diffusion equation, using neoclassical resistivity, constrained to match the EFIT reconstructed separatrix and total plasma current, with a flat $Z_{\rm eff}$ profile. The diffusivity was obtained from a separate code utilizing a fine radial grid, in general magnetic geometry,

$$D_{\rm eff} = \frac{V_{\rm Ware}\langle|\nabla\rho|\rangle + \frac{1}{n_e}\frac{1}{V'}\int d\rho\, V' \frac{\partial n_e}{\partial t}}{\langle|\nabla\rho|^2\rangle \frac{d\ln n_e}{d\rho}}, \qquad (2)$$

where ρ is the normalized square root of toroidal flux, $V(\rho)$ is the flux surface volume, $\Gamma_{\rm Ware} = n_e V_{\rm Ware}$, and $\langle\rangle$ is the flux-surface average.

The result $D_{\rm eff} > 0$, for all time and all radii, confirms that the Ware pinch is sufficient to account for the density rise [6, 33], leaving a margin for outward turbulent diffusion. The ITB is centered at $\rho = 0.4$ as defined by the radius of shortest density gradient scale length, and is localized to a relatively narrow radial region (sawtooth heat pulse analysis suggests the electron thermal ITB is even more narrow [6]). The diffusivity could not be accurately inferred in the flat density gradient region outside the half-radius and is therefore not shown.

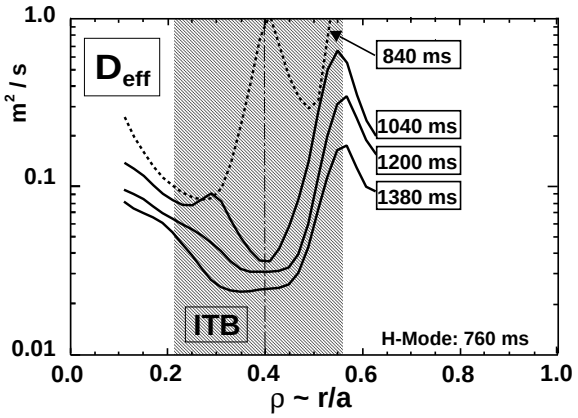

FIG. 3: Radial profiles of the effective diffusivity inferred from the measured density profiles of Fig. 2 and the calculated Ware pinch. Profiles are shown just after the H-Mode transition (840 ms), at the end of the ITB formation (1040 ms), just before on-axis ICRH (1200 ms), and during on-axis heating (1380 ms).

III. TEM STABILITY AND LINEAR GYROKINETIC ANALYSIS

The GS2 code solves the gyrokinetic Vlasov-Maxwell equations as an initial value problem, using the ballooning representation for linear cases, and a radially local, flux tube simulation domain [34], for nonlinear cases. The solution method is fully implicit for linear terms and explicit for nonlinear terms. Gaussian quadrature integration is employed throughout the code to increase accuracy. The flux tube representation extends along the magnetic field, with a cross-section of order $60\rho_i \times 60\rho_i$ at the outer midplane, where ρ_i is the ion gyroradius, and employs radially periodic "twist and shift" boundary conditions. The code solves for an arbitrary number of gyrokinetic plasma constituents, and is fully electromagnetic (only electrostatic results are presented here; electromagnetic effects are negligible in these low β cases). The magnetic geometry can be input as either a numerical equilibrium obtained from an equilibrium fitting code such as EFIT, or various analytical forms. In this work, we use the Miller equilibrium representation, [35], which specifies the beta, shift, midplane radii, elongation, and triangularity on a given flux surface, together with their gradients, which are used to obtain an approximate equilibrium solution in the vicinity of the flux surface. We have developed interface and plotting software GS2_PREP [5] and GS2_PLOT to automatically prepare, execute, and plot a collection of GS2 runs for all radii and times of interest (used to automatically prepare Fig. 5 below), as well as parameter scans, from TRANSP [36] input. TRANSP analysis is routinely performed for tokamak experiments worldwide. We have benchmarked our linear stability analysis, for both toroidal ITG and trapped electron modes, against independent analyses using the FULL code [37] in JT60-U ITB cases, and against the GKS code for DIII-D pellet enhanced performance modes [38]. The simulations presented here employ three gyrokinetic species (deuterons, electrons, and an impurity - boron), 16 energy grid points, 20 circulating particle pitch angles, and 32 trapped particle pitch angles. The magnetic shear parameter $\hat{s} = (r/q)dq/dr = 0.685$ is relatively weak, so that TEMs are extended along field lines, requiring three ballooning angle periods to encompass the eigenfunctions. Simulations in Figs. 4, 5, 7, 8, 9, and 11(b) were inadvertently carried out using oxygen as the impurity and with the deuterium collisionality erroneously large. We have confirmed these differences have no significant effect on the linear results. All other linear and nonlinear simulations have been corrected, particularly where comparisons with experiments are made.

Figure 4 shows the evolution of the maximum linear growth rate as calculated using the GS2 code, at the center of the ITB ($\rho = 0.4$), where the inverse density gra-

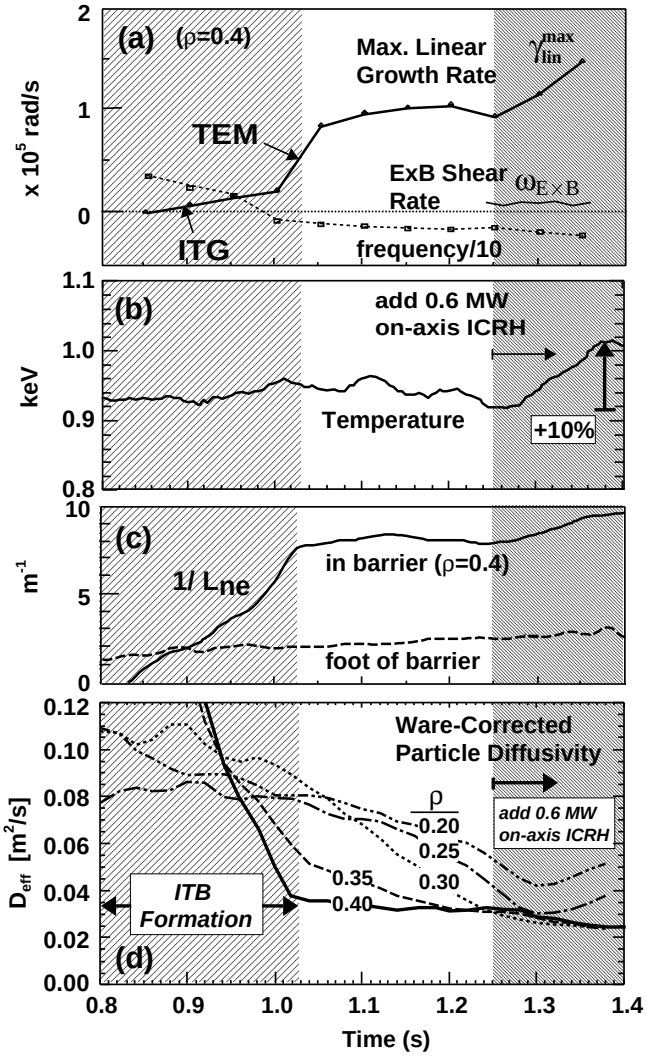

FIG. 4: Temporal evolution of (a) maximum linear growth rate, radial electric field shearing rate, and real frequency, at the ITB radius ($\rho = 0.4$); (b) temperature at the ITB radius; (c) inverse density gradient scale length $L_{ne}^{-1} = -d\ln n_e/dr$ evaluated from visible bremsstrahlung data; (d) Effective particle diffusivity $D_{\rm eff}$ inside the ITB foot, inferred from density profile measurements and the calculated Ware pinch.

dient scale length, $L_{ne}^{-1} = -d\ln\, n_e/dr$, is maximum (the midplane minor radius is approximately 22 cm). Also shown are the temperature, which increases 10% during on-axis heating, the inverse density gradient scale length, and the effective electron particle diffusivity $D_{\rm eff}$ from Eq. (2) (corrected for the Ware pinch), at the same radius. The toroidal ITG mode remains marginally stable until 0.83 seconds, following the H-Mode transition, even as the temperature gradient steepens. From 0.83 seconds to 1.00 seconds, trapped-electron ion temperature gradient driven modes [39] are weakly unstable, following a trajectory where a/L_T, the normalized inverse temperature gradient scale length, is nearly constant. Before 1.00 seconds, little particle transport is expected (nonlinear simulations are shown later); the density and potential perturbations must be out of phase to produce particle transport. The weakly growing trapped-electron-ITG modes present in the ITB before 1.00 seconds are characterized by a nearly adiabatic electron response.

Because the Ware pinch is sufficient to produce the observed density rate of rise in the absence of significant particle transport, the ITB forms. The inferred marginal stability of toroidal ITG modes may result from self-consistent profile changes associated with $E \times B$ shear, or more directly, from broadening of the temperature profile by off-axis heating. The latter brings the temperature gradient near or below the critical value. The details of formation remain to be addressed in future work that can exploit recently improved profile measurements (electron temperature from ECE, density from Thomson scattering, turbulence measurements, and potentially q-profiles from MSE). A separate investigation of this early phase, based on the same data, also finds no unstable modes inside the ITB foot [40].

As the density gradient steepens during ITB formation, trapped electron modes are driven unstable. At approximately 1.00 seconds, the TEM stability boundary is crossed and the phase velocity changes to the electron direction. This coincides with the time that L_{ne} comes to steady state, and the end of the ITB formation phase. As will be shown in the following, a/L_{ne} is the sole driving factor for trapped electron modes in this regime. At the same time, the particle diffusivity obtained from Eq. (2) ceases to decrease. This suggests that the onset of trapped electron modes, which produce strong particle transport relative to toroidal ITG modes, may limit the ITB density rise. Late in the discharge, the growth rate of the TEM increases further, suggestive of the deleterious role played by on-axis heating. The diffusivity $D_{\rm eff}$ increases for radii inside $\rho = 0.35$ during on-axis heating. The slight decrease of $D_{\rm eff}$ at $\rho = 0.4$ during on-axis heating could be misleading. Because the inverse density gradient increases, the turbulent flux actually increases.

Also shown in Fig. 4 is the ExB shearing rate from radial force balance, including the pressure gradient. The impurity toroidal velocity was obtained from a parabolic fit that falls within error bars of more recent HIREX data for three radii [41, 42] (near the axis, one-third radius, and two-thirds radius) and the poloidal rotation from a numerical neoclassical calculation [5, 43, 44]. The shearing rate is much smaller than the growth rate late in the discharge. As shown in Fig. 1, the toroidal rotation changes sign as the ITB forms and again during on-axis heating, where it becomes small. In the impurity radial force balance, the pressure gradient term is dominant during on-axis heating, while the poloidal rotation term remains small. This allows the radial electric field to be obtained during on-axis heating without detailed profile data for the toroidal velocity. Because the toroidal rotation is important before on-axis heating, and its profile is unknown, the shearing rate cannot be reasonably determined for earlier times. Preliminary indications are that

an E_r well forms near the foot of the ITB, creating a local peak in the $E \times B$ shearing rate near the ITB foot (half-radius), where the maximum linear growth rate is small.

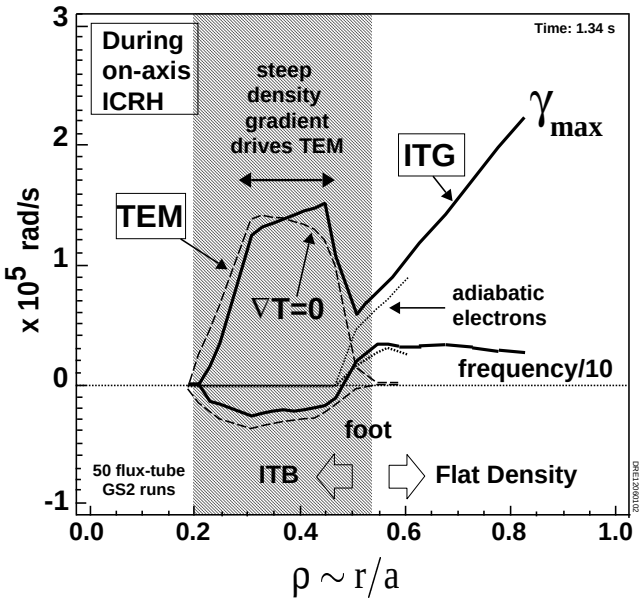

FIG. 5: Profiles of the linear growth rate (maximized over $k_\theta \rho_i$) at 1.34 seconds, during on-axis ICRH. The mode in the ITB is insensitive to the temperature gradient (driven by the density gradient), has a phase velocity in the electron direction, and disappears with adiabatic electrons only. The mode outside the ITB foot is driven by the temperature gradient, is well-described by adiabatic electrons, and has a phase velocity in the ion diamagnetic direction.

Figure 5 shows the radial profile of the maximum linear growth rate calculated in 50 GS2 runs, at 1.34 seconds, during on-axis ICRH. A strongly growing mode appears inside the ITB foot, with a phase velocity in the electron direction ($\omega_r < 0$). Artificially turning off the temperature gradient does not affect the maximum growth rate, showing the mode is driven solely by the density gradient. The mode disappears when only adiabatic electrons (Boltzmann response) are included, and is therefore associated with trapped electrons. Outside the ITB foot, the phase velocity is in the ion diamagnetic direction, and the growth rate is not significantly reduced with adiabatic electrons. This mode can be identified as the toroidal ITG mode, and has a growth rate increasing with minor radius as is typical of H-Mode plasmas.

Two types of trapped electron modes were initially discovered [45–47]. The "dissipative trapped electron mode" (DTEM) is an electron drift wave driven unstable by the nonadiabatic electron response produced by detrapping, with effective collision frequency $\nu_{\rm eff} = \nu_{\rm ei}/\varepsilon$, where $\nu_{\rm ei}$ is the electron-ion collision frequency and $\varepsilon = r/R$ is the inverse aspect ratio. The DTEM has a growth rate initially increasing with collision frequency (eventually decreasing with collision frequency when ion-ion collisions introduce damping). The destabilizing effect of electron-ion collisions is opposite our results, and only appears for collision frequencies much larger than those in the C-Mod experiments. The more relevant collisionless trapped electron modes [47], driven unstable by resonance with the trapped electron toroidal precession drift were also discovered, and shown to be unstable beyond a critical density gradient, $r/L_n > (1/3)\sqrt{r/R_0}$, with a growth rate $\gamma \simeq \varepsilon^{1/4}\omega_*(1+\eta)/\sqrt{2}$, where $\omega_* = k_\theta \rho_i v_{\rm thi}/L_n$ with $v_{\rm thi}$ the ion thermal velocity, and $\eta = L_n/L_T = d\ln T/d\ln n$. The poloidally local stability analysis of the collisionless TEM was later revisited [48], for perturbations about $\omega \simeq \omega_*$, both analytically and numerically, neglecting ion magnetic curvature and ∇B drifts. The resulting growth rate (correcting errors) is $\gamma = 2\pi\,\omega_*\eta_e(n_T/n)^{1/2}x_0^{1/2}(x_0 - 3/2)\exp(-x_0)$, where $x_0 = R/L_nG$, $n_T/n = (2/\pi)\sqrt{2\varepsilon}$ is the flux surface averaged trapped particle density, $\varepsilon = r/R_0$, and $G \simeq 1.2$. All of the modes we find have $\omega < (L_n/R)\omega_* \ll \omega_*$, so that these results are not directly applicable. Nevertheless, some trends remain qualitatively consistent, for example, we observe the stabilizing effect of temperature gradients at shorter wavelengths, which results from a finite gyroradius induced downshift of the real frequency. A more complete ballooning perturbative analysis reported good agreement with numerical solutions, as reported in Ref. [49].

Non-resonant, "fluid-like" trapped electron modes are driven unstable by the trapped electron precession drift in the bad curvature region [50, 51]. Incidentally, the toroidal ITG mode in the fluid limit was also discovered in the same work [2]. The simplest dispersion relation is obtained by expanding the trapped electron kinetic response for $\omega_{De}/\omega \ll 1$, where $\omega_{De} = \omega_{*e}L_n/R$ is the curvature drift frequency. Not reliant upon a small class of resonant particles, these robust modes were proposed to explain electron thermal energy transport [52]. The real part of the frequency is a function of poloidal wavenumber, and changes sign (from the electron to ion direction) for shorter wavelengths. The non-resonant modes are clearly present in the spectra we calculate. At a minimum, these modes appear at shorter wavelengths where the frequency changes sign, where a subclass of the modes is purely growing (therefore *cannot* be resonant). A numerical study of both the resonant and non-resonant modes was presented in Ref. [53].

Most transport modeling has considered regimes with relatively peaked ion temperature profiles, where the toroidal ITG mode dominates, and trapped electrons are a small additional destabilizing mechanism [9, 54] which tends to "soften" or lower the critical ion temperature gradient (most recently confirmed in Ref. [55]). The C-Mod cases we consider, however, are in the more extreme range of density gradients, where the TEM is driven almost purely by the density gradient rather than the temperature gradient. This is also simplifying in the sense that the particle transport remains diagonal, rather than off-diagonal.

The following approximate expression for the growth rate, in the fluid limit, can be readily derived, starting from the kinetic ion response given in Eq. (2) of Ref. [56], and expanding the trapped electron response of Ref. [48] for $\omega_{De}/\omega \ll 1$, in the local approximation, for $\eta_i \gg 1$ and $\eta_i \ll 1$, where $\eta_i = d\ln T_i/d\ln n$, $b_i = k_\theta^2\rho_i^2/2$, n_{eT} is the trapped electron density, $n_i = n_e = n$, and $T_i = T_e$ have been assumed for simplicity, and $g_{\rm eff} = v_{\rm thi}^2/R$,

$$\gamma \simeq k_\theta \rho_i \Big(\frac{g_{\rm eff}}{L_n}\Big)^{1/2} \Big(\frac{(1+\eta_e)n_{eT}/n + \eta_i}{1 - n_{eT}/n + b_i}\Big)^{1/2} \qquad (3)$$

This expression, while heuristic, qualitatively captures several features of the TEM and ITG modes in the fluid limit. For example, the TEM (associated with n_{eT}/n) becomes important when $\eta_i \ll 1$, and plays a smaller role when the toroidal ITG mode (last term) is strongly growing. Eq. 3 also illustrates the bad curvature drive mechanism in the fluid limit. However, it is not valid near threshold or for the resonant modes, which are important as well.

The linear growth rate spectrum late in the discharge, at the ITB radius, is shown in Fig. 6(a). The phase velocity is in the electron direction, the spectrum peaks at $k_\theta\rho_i = 0.6$, is extended to relatively short wavelengths $k_\theta\rho_i = 2.3$, and the shorter wavelengths are almost purely growing. The temperature gradient has a *stabilizing* influence on the shorter wavelength modes [2, 48, 53]. Figure 6(b) shows the root-locus diagram for the same data shown in 6(a), as $b = k_\theta^2\rho_i^2$ varies. Frequencies are normalized to the electron curvature drift frequency $\omega_{De}/\sqrt{b}$. Both resonant modes and non-resonant modes are present in the spectrum.

Before moving on to nonlinear turbulence simulations, we consider the increase of the TEM critical density gradient with the temperature gradient mentioned in Ref. [48]. We have used a large number of linear GS2 simulations to map out the stability diagram in a/L_n vs. a/L_T space. For parameters characterizing ρ=0.4 at 1.20 seconds, the TEM threshold was fit by a line, $(a/L_n)_{\rm crit} = 0.4 + 0.83(a/L_T)$ for $0 \le a/L_T \le 1.45$, and a constant $(a/L_n)_{\rm crit} = 1.6$ for $a/L_T \ge 1.45$. Because $a/L_T \ge 1.5$ for $t \ge 0.80$ seconds, on-axis heating does not affect the TEM linear critical density gradient.

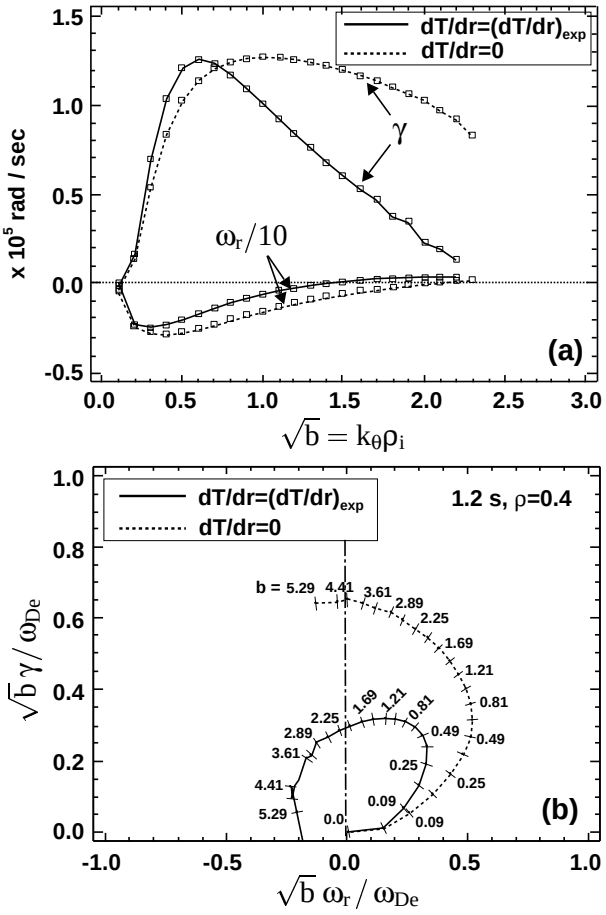

FIG. 6: (a) Linear growth rate spectrum at 1.20 seconds, $\rho = 0.4$ in the ITB, compared to the same with the temperature gradient set artificially to zero. The temperature gradient suppresses shorter wavelength modes. (b) Root locus for the same cases, showing the existence of both resonant and purely growing ("fluid-like") modes. Here $k_\theta\rho_i$ does not contain the $\sqrt{2}$ factor, so that b is equal to the customary value; ω_{De} is the magnetic drift frequency.

IV. NONLINEAR SIMULATIONS OF TEM TURBULENCE IN THE ITB

A. Increase in turbulent diffusivity during on-axis heating

Nonlinear simulations of TEM turbulence are made more difficult than simulations of ITG turbulence in part by the extended $k_\theta\rho_i$ spectrum. This results in eigenmodes that extend considerable distances in ballooning angle, requiring an extended radial wavenumber spectrum to resolve. Because the cross-section of the simulation domain follows the shear of the magnetic field lines, a rectangular cross-section at the outer midplane becomes a flattened parallelogram as one moves in the parallel direction. It is easy to show that the radial wavenumber is related to the poloidal wavenumber via $k_x = \hat{s}\theta k_y$, where θ is the parallel angle-like coordinate, and $\hat{s} = d\ln q/d\ln r$ is the magnetic shear parameter. Our convergence studies indicate that roughly eight times as many radial modes are required as poloidal modes, counting both positive and negative k_x. Using significantly less radial modes resulted in lower transport and an erroneously large pinch in the early ITG/TEM phase. Further, at least 11 poloidal modes ($k_\theta\rho_i$ values) are required. Simulations running roughly 300 μsec, with 11 poloidal and 85 radial modes, require 24 hours on 2640 processors on the National Energy Research Supercomputer Center (NERSC) International Business Machines model SP/2. Similar results were obtained for the case before on-axis heating, using roughly half the number of

modes in each direction, yielding runs 1.1 ms in duration in 8 hours on 720 processors. On this basis, we carried out parameter scans at the lower resolution and detailed comparisons with experiments at the higher resolution.

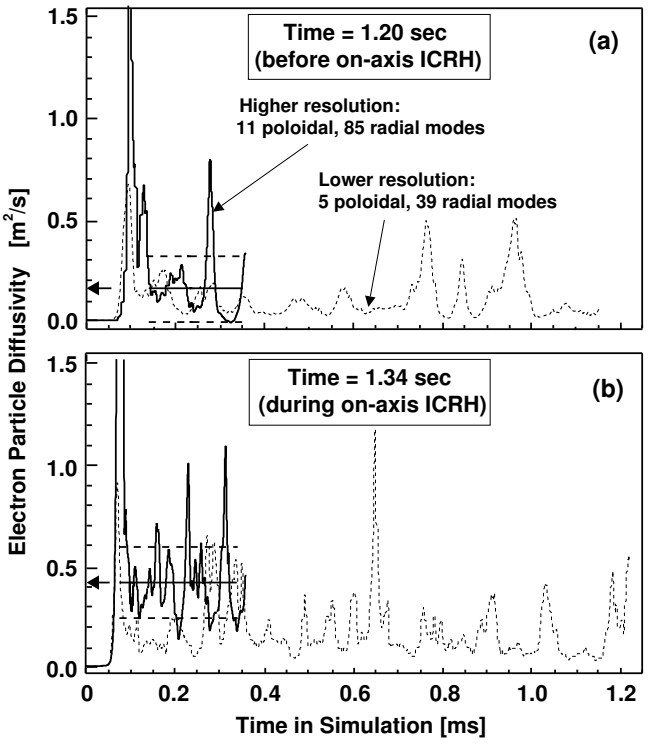

FIG. 7: (a) Simulated electron particle diffusivity from GS2 at 1.20 seconds, $\rho = 0.4$, assuming flat $Z_{\rm eff}$ profile, for high and low k-space resolutions. The high resolution result is 0.25 m^2/s. (b) The same at 1.34 seconds. The high resolution result is 0.4 m^2/s, demonstrating an increase in simulated particle diffusion during on-axis ICRH. Dashed lines indicate the error on the estimate of the mean as a crude characterization of the intermittency.

Figure 7(a) compares high and low resolution simulations at 1.20 seconds (before on-axis ICRH), at the ITB radius $\rho = 0.4$. A flat $Z_{\rm eff}$ profile was assumed, taking the density gradient scale length directly from the VB emission profile. Even the longer duration simulation shows large, infrequent bursts of particle flux occur throughout the simulation. These bursts result from transient suppression and recovery of the zonal flows, whose growth rate is proportional to the amplitude of the primary modes, in response to nonlinear interaction with the primary modes. We face choosing between better physics (better resolution in k-space), and better statistics (longer run time) for averaging. Figure 7(b) shows the same comparison at 1.34 seconds, during on-axis heating. The increase in TEM turbulent diffusivity during on-axis heating is apparent, and does not originate from changes in the linear stability threshold.

B. Nonlinear simulations of ITB trajectory

Initially, we explore the qualitative behavior of the turbulent particle flux using nonlinear GS2 simulations with 5 poloidal modes, holding all parameters except the density gradient fixed at $\rho = 0.4$ and 1.20 seconds. Figure 8 (a) shows the maximum linear growth rate and real frequency as a function of driving factor, a/L_{ne}, indicating $(a/L_{ne})_{\rm crit} \simeq 1.2$. Frame (b) shows the GS2 electron particle diffusivity, due to TEM turbulence, as a function of driving factor, a/L_{ne}. The horizontal axis can be thought of as time along the ITB trajectory; beyond 0.80 seconds, a/L_T remains betwen 1.5 and 1.7. Initially there is a very small anomalous pinch. Orders of magnitude smaller than the Ware pinch, it appears only while $\eta_e > 2$, and is 80% due to circulating particles, as indicated by the flux as a function of pitch angle. This is consistent with a passing electron resonant effect described by Hallatschek [57]. The effect is very small in the high density plasmas we consider, presumably as a result of collisional broadening. As the density gradient increases, η_e falls below 2 and the pinch vanishes. At 1.00 seconds, the linear critical density gradient $a/L_{ne} = 1.2$ is exceeded. However, no turbulent diffusion appears until the density gradient steepens significantly further. The turbulent particle flux near marginal stability, Fig. 8(c), is quasi-periodic with a period roughly 20 linear growth times. Far above marginal stability, Fig. 8(d) shows the flux becomes much more irregular, and displays a finer temporal structure, consistent with higher growth rates farther above threshold. Examination of the zonal flow potentials near marginal stability reveals bursts of energy exchange with the dominant primary mode, lagging the bursts in particle flux.

C. Nonlinear upshift of TEM critical density gradient

The nonlinear upshift alluded to in Sec. IV B, in the critical *density* gradient for TEM turbulence, has not been previously reported. An analogous shift in the critical temperature gradient has been observed for toroidal ITG turbulence with adiabatic electrons [1] ("Dimits shift"). The latter shift arises from turbulence self-quenching by zonal flows.

Here we investigate the upshift in detail, using high resolution simulations, with 11 poloidal modes and 85 radial modes. Figure 9 shows the particle flux, particle diffusivity, and electron thermal diffusivity from GS2 as a function of a/L_{ne}, with all other parameters held constant, at their $\rho = 0.4$, $t = 1.20$ second values. It is clear that the turbulent fluxes are negligible between the linear threshold, $a/L_{ne} = 1.20$, and $a/L_{ne} \simeq 1.34$, after which they strongly increase. We have used the rms variance throughout to crudely indicate the degree of intermittency in the simulation results. It is clear from Fig. 8(c) that the probability distribution function is

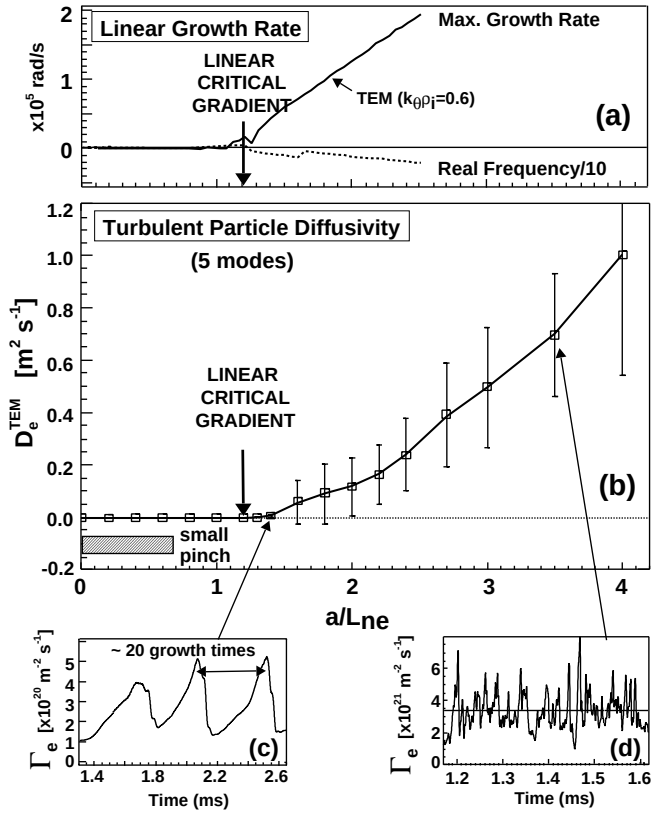

FIG. 8: Nonlinear simulations, holding all other parameters fixed at 1.20 seconds and $\rho = 0.4$, varying a/L_{ne}. (a) Max. linear growth rate and real frequency. (b) Simulated diffusivity due to TEM turbulence. The x-axis can be thought of as time along the ITB trajectory. Initially there is a very small anomalous pinch. Turbulent diffusion does not appear until the linear critical gradient is exceeded by some margin. (c) Turbulent particle flux very near marginal stability is quasi-periodic, and (d) much less regular far above marginal stability.

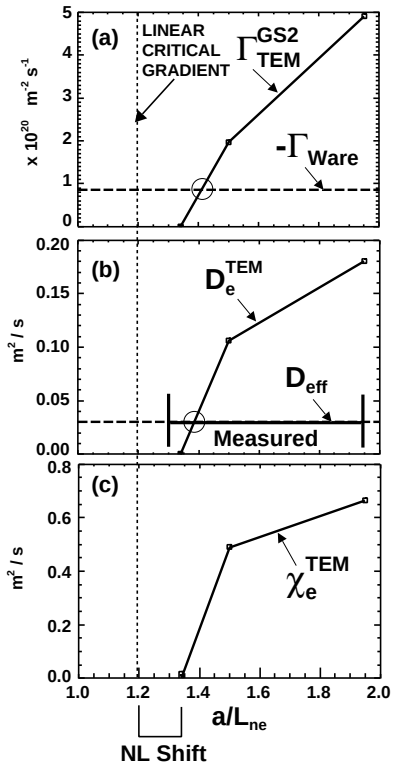

FIG. 9: Details of a/L_{ne} scan near threshold. Simulated and measured particle and energy transport at 1.20 seconds, at $\rho = 0.4$, from high resolution GS2 simulations, other parameters held constant, with flat $Z_{\rm eff}$ profile. (a) TEM particle outflux balances Ware pinch at $a/L_{ne} \simeq 1.4$. (b) TEM particle diffusivity matches $D_{\rm eff}$ from transport analysis at $a/L_{ne} \simeq 1.4$, within the range of uncertainty in measured a/L_{ne}. (c) Simulated electron thermal diffusivity χ_e.

non-Gaussian, so the rms variance is not a quantitative measure of the intermittency.

The results for $(a/L_{ne}, D_{\rm eff}[{\rm m}^2/{\rm s}])$ are (1.34, 5.55e-04 +/- 2.23e-04), (1.56, 0.114 +/- 0.112), and (1.95, 0.180 +/- 0.050). The "measured" horizontal error bar on the plot indicates the possible range of a/L_{ne} in the experiment given uncertainty in the $Z_{\rm eff}$ gradient, discussed in more detail in the next section. Frame (a) shows the particle flux from GS2 is equal to the Ware pinch for $a/L_{ne} = 1.4$. Frame (b) shows the simulated particle diffusivity is equal to the $D_{\rm eff}$ inferred from Eq. (2), at the same value of $a/L_{ne} = 1.4$. Finally, frame (c) shows the electron thermal diffusivity χ_e^{TEM} is equal to the value computed by TRANSP within uncertainty. Note that $\chi_e^{\rm TEM} > D_e^{\rm TEM}$. In these comparisons, the $Z_{\rm eff}$ gradient was neglected. The effect of varying the $Z_{\rm eff}$ gradient is considered in detail in Sec. IV D.

The shift in TEM critical density gradient likely arises from the fact that the zonal flow growth rate is proportional to the primary mode amplitudes, leading to explosive instability, combined with the observation that a component of the zonal flow remains undamped [58]. A theory for the Dimits shift in ITG turbulence, invoking zonal flow damping by tertiary modes, has been proposed [59] for the case of adiabatic electrons, but is not directly applicable. From this increase in turbulent diffusivity above a critical inverse density gradient scale length, it is apparent that TEM turbulence will limit the density peaking by opposing the Ware pinch, once this nonlinear threshold is exceeded.

D. Comparison of simulated and measured particle and heat transport

To compare simulated transport with that inferred from the experiments, it is necessary to account for uncertainty in the gradient of $Z_{\rm eff}$. From fits to more recent ITB data with improved Thomson scattering radial resolution, the $Z_{\rm eff}$ profile appears to peak slightly off-axis, and is approximately flat outside the ITB foot. Accordingly, the upper limit of possible a/L_{ne} values is ob-

tained by assuming flat $Z_{\rm eff}$ at the radius of interest, yielding $a/L_{ne} = 1.95$ directly from the calibrated VB emission profile $n_e\sqrt{Z_{\rm eff}}$. The lower limit on a/L_{ne} is found by assuming that at worst, $Z_{\rm eff}$ has a gradient scale length as short as that of the electron density. Using $L^{-1}_{n_e\sqrt{Z_{\rm eff}}} = L^{-1}_{n_e} + L^{-1}_{Z_{\rm eff}}/2$ gives a reduction in the inferred a/L_{ne} by 2/3.

Next we perform a scan of a/L_{ne}, at 1.20 seconds and $\rho = 0.4$, encompassing the linear critical gradient for TEM onset and the upper limit of the experimentally measured a/L_{ne}. The gradient of $n_e {Z_{\rm eff}}^{1/2}$ is held fixed at the measured value. In the GS2 simulations, the deuterium, impurity, and electron density gradient scale lengths are self-consistently adjusted as a/L_{ne} is varied, to account for the $Z_{\rm eff}$ gradient while maintaining charge neutrality. All other parameters, including $Z_{\rm eff}$, are held constant. For values of $a/L_{ne} < 1$, the impurity density profile is so peaked that the deuterium density gradient is inverted (no inversion occurs within the range of measured a/L_{ne}). The changing $Z_{\rm eff}$ gradient is also accounted for in the $D_{\rm eff}$ and has no significant effect on the Ware flux or TRANSP $\chi_{\rm eff}$.

Figure 10 shows the comparison between simulation and experiment. The TEM turbulent particle flux balances the Ware pinch, and the TEM diffusivity equals the $D_{\rm eff}$ inferred from Eq. (2) when $a/L_{ne} \simeq 1.47$, well within the range of experimental uncertainty in a/L_{ne}. The TEM turbulent electron thermal diffusivity matches the TRANSP value at a slightly larger $a/L_{ne} \simeq 1.8$, also well within the experimental uncertainty. It is worth pointing out that the TRANSP χ_e involves calculation of the heating profile from TORIC [60], simplified by taking only one parallel wavenumber in the antenna spectrum, which results in a more narrow deposition profile than the full spectrum. Estimated error in computing the heating profile is roughly $\pm 10\%$. In addition, the strong ion-electron coupling in these high density plasmas makes it difficult to infer χ_e and χ_i separately without large uncertainty. Because we have taken $T_e = T_i$ in the transport analysis, forcing the electron-ion energy exchange to zero, the size of this term is unknown, and we cannot separate χ_e from χ_i. We have chosen to compare against an effective fluid diffusivity that arises naturally when the energy balance equations for electrons and ions are summed, which removes the ion-electron energy exchange term. We have evaluated $\chi_{\rm eff} = (q_e + \sum_i^{th} q_i)/(n_e T_e' + \sum_i^{th} n_i T_i')\langle|\nabla\rho|\rangle$ using the total heat flux from TRANSP, and also from GS2, and the same denominator in both cases. The heat flux absorbed by ions is negligible for $\rho < 0.4$, with significant ion power density only between $\rho = 0.4$ and $\rho = 0.6$. The neoclassical ion heat flux at $\rho = 0.4$ is 6 W/cm^2, compared to the total heat flux of 27 W/cm^2. If the neoclassical flux were added to the GS2 result, the resulting $\chi_{\rm eff}$ would be 22% larger, reducing the a/L_{ne} at which $\chi_{\rm eff}$ matches TRANSP.

The comparison of particle fluxes involves no external models other than the neoclassical Ware flux calculation. Nevertheless the a/L_{ne} value at which agreement on $\chi_{\rm eff}$ is obtained falls within 15% of the value at which $D_{\rm eff}$ agrees. From this we conclude that the simulated fluxes agree with experimental measurements within error bars.

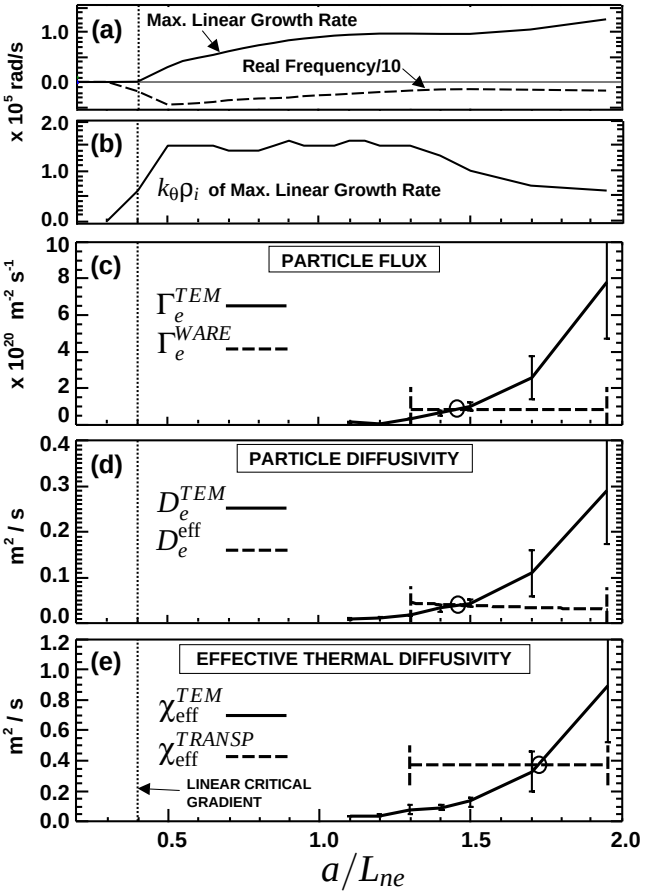

FIG. 10: Comparison of simulated and measured transport, at $\rho = 0.4$, $t = 1.2$ seconds, accounting for $Z_{\rm eff}$ gradients. (a) Max. growth rate and real frequency as functions of a/L_{ne} from linear GS2 simulations. (b) Poloidal wavenumber $k_\theta\rho_i$ yielding the max. linear growth rate. (c) Particle flux from TEM turbulence equals the Ware pinch for $a/L_{ne} \simeq 1.47$, within the experimental error. (d) Particle diffusivity from TEM turbulence equals $D_{\rm eff}$ from Eq. (2) for $a/L_{ne} \simeq 1.47$, within the experimental error. (e) Simulated effective thermal diffusivity $\chi_{\rm eff}$ matches TRANSP thermal diffusivity $a/L_{ne} \simeq 1.72$. All matching values of a/L_{ne} fall within experimental error bars of measured a/L_{ne} and within 15% of each other.

Finally, we have not included electron temperature gradient (ETG) driven modes in the simulations for two reasons. First, evaluating a fit to the ETG critical temperature gradient [61] shows that ETG modes are stable inside the ITB foot, due to the large density gradient. Outside the ITB foot, where the density profile is flat, ETG modes are predicted to be unstable. Even if ETG modes were unstable in the ITB, negligible particle transport would result. This can be understood from the fact that the wavelength for ETG modes is much shorter than the ion gyroradius, so that the ions tend to average away the perpendicular fluctuations and behave adiabatically

[47]. However, if ETG turbulence led to significant electron thermal transport [4], the agreement between $\chi_{\rm eff}$ and experiments would be further improved.

V. MECHANISM FOR ITB CONTROL WITH ON-AXIS HEATING

It appears that the density gradient increases until the TEM turbulent diffusion balances the Ware pinch. i.e., $\Gamma_{\rm Ware}+\Gamma_{\rm TEM}=0$, which implies $\partial_t n_e = 0$. The restoring force, arising from the increase of TEM particle flux with the density gradient, results in a stable equilibrium.

The main effect of on-axis heating is to increase the temperature at the ITB radius by 10%, as shown in Fig. 4(b). This results in a -20% decrease in collisionality at $\rho = 0.4$. The question then arises as to whether this decrease in collisionality is accompanied by a significant increase in TEM transport. Figure 11(a) shows the results of an artificial scan of the collisionality up to the experimental value during on-axis heating. Initially, there is a very strong dependence of the linear growth rate on collisionality, but this dependence appears to be saturated near the experimental value of 0.44. Fig. 11(b) shows the results of a temperature scan carried out nonlinearly. It is clear that the effect of changes in collisionality is weak and temperature scaling of the TEM turbulent diffusivity is dominated by gyroBohm scaling $D_{\rm eff}^{\rm TEM} \propto T^{3/2}$. Note the size scaling obtained from the flux-tube code GS2 must be gyroBohm; accounting for profile variation may give a scaling between Bohm ($\propto T$) and gyroBohm ($\propto T^{3/2}$). Here $\rho_* = \rho_i/a = 1/188 = 0.0053$, which we expect is not large enough to cause major departures from gyroBohm scaling. In addition, equilibrium $E\times B$ shear is weak [10] and should have little impact on the transport scaling. Nevertheless, if the scaling were more Bohm-like in character, our conclusions would remain unaffected. The Ware pinch displays its strongest sensitivity to collisionality for ν_{*e} in the vicinity of $\nu_{*e} \simeq 0.8$ characterizing these experiments. In addition, the plasma current is maintained by feedback, so that resistivity results in the toroidal electric field decreasing with temperature, $E_\zeta \propto T^{-3/2}$. The two effects together cause the Ware pinch to decrease slightly faster than $T^{-1/2}$.

The temperature dependence arising from collisionality changes is weaker than gyroBohm scaling, for TEM turbulence. This leads us to conclude that the main mechanism for ITB control with on-axis ICRH is the increase in TEM turbulent diffusivity due to the generic unfavorable temperature scaling of turbulent transport (gyroBohm), together with the unfavorable (weaker) temperature scaling of the Ware pinch. In both temperature scalings, collisionality dependence, unfavorable for TEM transport, and favorable for Ware pinch, plays a second-order role. However, we point out that the incremental effect of increasing the electron collisionality is very strong for small collisionalities, so that simulations of TEM turbulence that do not include at least some electron-ion collisions are unrealistic.

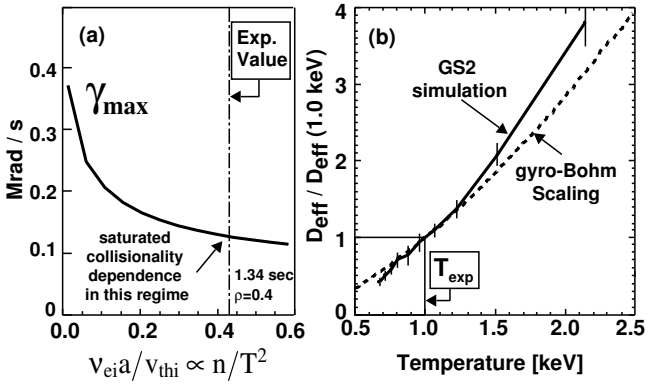

FIG. 11: (a) Dependence of maximum linear growth rate on collisionality, for $\rho = 0.4$ at 1.34 seconds, is saturated in the high density C-Mod ITB. (b) The simulated turbulent diffusivity has a temperature dependence dominated by gyroBohm scaling with a 2^{nd} order effect of collisionality.

VI. CONCLUSIONS

In summary, we have shown that the neoclassical (collisional) Ware pinch is sufficient to form C-Mod internal particle (and energy) transport barriers if anomalous transport is sufficiently reduced. Our gyrokinetic stability analysis at the ITB radius indicates that toroidal ITG modes (with slight additional destabilization by trapped electrons – "ITG/TEM") are marginally stable immediately following the transition to EDA H-Mode, which may be consistent with broadening of the temperature profile by off-axis heating. This allows the Ware pinch to peak up the density profile inside the heating radius. As the density profile peaks, it eventually exceeds the critical density gradient for trapped electron modes. These modes are driven both by toroidal precession drift resonance and by non-resonant fluid-like mechanisms in the bad curvature region. The end of the ITB formation phase was observed to coincide with the calculated onset of trapped electron modes. Nonlinear turbulence simulations reveal a new nonlinear upshift, associated with zonal flows, in the critical density gradient for the onset of TEM turbulent transport. The outward particle flux increases rapidly after this nonlinear critical density gradient is exceeded, until it balances the Ware pinch, leading to a stable equilibrium. Applying on-axis ICRH increases the temperature. This equilibrium is sensitive to temperature mainly through the gyroBohm scaling of turbulent transport. In the particular experiments studied, this equilibrium is established in the steep gradient region ($\rho = 0.4$). At the time on-axis heating is applied, $D_{\rm eff}$ is still decreasing with time inside this radius, because the TEM are less virulent there. When the on-axis heating is applied, the TEM turbulent diffusion increases

in this inner core region to arrest the density rise.

We also observe that for our simulations of TEM turbulence, the electron thermal, impurity particle, electron particle, and ion thermal diffusivities are ordered $\chi_e > D_I > D_e > \chi_i$, so that TEM turbulence is an effective means of removing impurities without degrading ion thermal energy content other than through the electron channel. In Alcator C-Mod, however, the ion-electron energy exchange time is much shorter than the energy confinement time, so that the TEM electron thermal transport may hinder both ion and electron temperatures enough to explain the lack of observed temperature profile peaking.

Finally, we speculate as to whether this mechanism applies to other transport barriers. Most other particle transport barriers are associated with reversed magnetic shear, which strongly reduces the growth rate of the TEM by reducing the effective number of trapped electrons in bad curvature [47]. However, if the density profile becomes steep enough, the TEM could become the limiting factor. The other question that arises is whether the C-Mod ITB will form when the current drive is non-inductive and there is no Ware pinch. These results suggest that it will not, because the circulating particle pinch is far too weak in C-Mod (Fig. 8). However, in higher temperature, lower density plasmas with initially peaked temperature profiles, the circulating particle pinch may well form an ITB in which the density gradient increases until $\eta_e = 2$. If the TEM critical density gradient is exceeded along this path, then we expect TEM turbulence to play a role. Similar transport barrier control has recently been demonstrated on the DIII-D tokamak, in the Quiescent Double Barrier regime [62] characterized by reverse magnetic shear. In that case, off-axis electron cyclotron heating results in flattening of the density profile, reducing impurity accumulation. This phenomenon was recently reproduced in JT60-U [63], and believed to be associated with flattening of the reverse shear q-profile caused by electron cyclotron current drive. Because the TEM is very sensitive to the degree of reversed magnetic shear, it may play a role in these experiments as well.

Acknowledgments

This work was supported by the U. S. Dept. of Energy. The C-Mod experiment is supported by U. S. Dept. of Energy Cooperative Agreement No. DE-FC02-99ER54512. Parallel computations of linear growth rates were performed on the 50 processor MIT PSFC Marshall Theory Cluster, while massively parallel nonlinear turbulence simulations were performed on the IBM SP/2 at the National Energy Research Supercomputer Center (NERSC) in Berkeley. It is a pleasure to thank Dr. Abhay Ram for managing our NERSC ERCAP proposals, T. Baker and Dr. J. Wright for their help maintaining the Marshall Theory Cluster, Prof. K. Molvig for enlightening discussions on the neoclassical pinch, and Prof. I. H. Hutchinson, Dr. J. Irby, Dr. D. Mossessian, Prof. R. Parker, Dr. S. M. Wolfe, and Dr. S. J. Wukitch for their comments and contributions to the experiments.

[1] A. M. Dimits, G. Bateman, M. A. Beer, *et al.*, Phys. Plasmas **7**, 969 (2000).
[2] B. Coppi and F. Pegoraro, Nucl. Fusion **17**, 969 (1977).
[3] M. Kotschenreuther, G. Rewoldt, and W. M. Tang, Comp. Phys. Comm. **88**, 128 (1995).
[4] W. D. Dorland, E. Jenko, M. Kotschenreuther, and B. N. Rogers, Phys. Rev. Lett. **85**, 5579 (2000).
[5] D. R. Ernst, R. E. Bell, M. G. Bell, *et al.*, Phys. Plasmas **7**, 615 (2000).
[6] S. J. Wukitch, R. L. Boivin, P. T. Bonoli, *et al.*, Phys. Plasmas **9** (2002).
[7] J. E. Rice, P. T. Bonoli, E. S. Marmar, *et al.*, Nucl. Fusion **42**, 510 (2002).
[8] W. Horton, Rev. Mod. Phys. **71**, 735 (1999).
[9] M. Kotschenreuther, W. Dorland, M. Beer, and G. W. Hammett, Phys. Plasmas **2**, 2381 (1995).
[10] D. R. Ernst, B. Coppi, S. D. Scott, M. Porkolab, and the TFTR Group, Phys. Rev. Lett **81**, 2454 (1998).
[11] O. Grüber, R. C. Wolf, R. Dux, *et al.*, Phys. Rev. Lett. **83**, 1787 (1999).
[12] T. Fujita, Plasma Phys. and Contr. Fusion **39**, B75 (1997).
[13] C. Gormezano, Y. F. Baranov, C. D. Challis, *et al.*, Phys. Rev. Lett. **80**, 5544 (1998).
[14] C. M. Greenfield, K. H. Burrell, J. C. DeBoo, *et al.*, Phys. Rev. Lett. **86**, 4544 (2001).
[15] J. E. Rice, R. L. Boivin, P. T. Bonoli, *et al.*, Nucl. Fusion **41**, 277 (2001).
[16] M. Kotschenreuther, W. Dorland, Q. P. Liu, G. W. Hammett, M. A. Beer, S. A. Smith, A. Bondeson, and S. C. Cowley, Sixteenth IAEA Fusion Energy Conference, Montreal, Canada, 7-11 October 1996, paper F1-CN-64/D1-5 (pub. IAEA, Vienna, 1997).
[17] ITER Physics Basis Editors, ITER Physics Expert Group Chairs and Co-Chairs, ITER Joint Central Team, and Physics Integration Unit, Nuclear Fusion **39**, 2137 (1999).
[18] R. Goldston, Plasma Physics and Controlled Fusion **26**, 87 (1984).
[19] I. H. Hutchinson, R. Boivin, F. Bombarda, *et al.*, Phys. Plasmas **1**, 1511 (1994).
[20] C. L. Fiore, J. E. Rice, P. T. Bonoli, *et al.*, Phys. Plasmas **8**, 2023 (2001).
[21] C. L. Fiore, P. T. Bonoli, D. R. Ernst, *et al.*, Bull. Am. Phys. Soc. **48**, 331 (2003), Paper UI1.004, submitted to Phys. Plasmas (2003).
[22] P. C. Efthimion, S. von Goeler, W. A. Houlberg, *et al.*, Phys. Plasmas **5**, 1832 (1998).
[23] W. P. West, M. R. Wade, C. M. Greenfield, *et al.*, Phys. Plasmas **9**, 1970 (2002).
[24] R. Budny, R. Andre, C. D. Challis, *et al.*, 30th EPS Conf. on Contr. Fusion and Plasma Phys., St. Petersburg, 7-11

July 2003 ECA Vol. 27, O-3.4A.
[25] E. J. Strait, L. L. Lao, M. E. Mauel, *et al.*, Phys. Rev. Lett. **75**, 4421 (1995).
[26] F. M. Levinton, M. C. Zarnstorff, S. H. Batha, *et al.*, Phys. Rev. Lett. **75**, 4417 (1995).
[27] L. Lao, H. S. John, R. D. Stambaugh, A. G. Kellman, and W. Pfeiffer, Nucl. Fusion **25**, 1611 (1985).
[28] R. J. Goldston, D. C. McCune, H. H. Towner, S. L. Davis, R. J. Hawryluk, and G. L. Schmidt, J. Comp. Phys. **43**, 61 (1981).
[29] M. A. Beer, G. W. Hammett, G. Rewoldt, E. J. Synakowski, M. C. Zarnstorff, and W. Dorland, Phys. Plasmas **4**, 1792 (1997).
[30] K. H. Burrell, Phys. Plasmas **4**, 1499 (1997).
[31] F. L. Hinton and R. D. Hazeltine, Rev. Mod. Phys. **48**, 239 (1976).
[32] S. Hirshman, Physics of Fluids **21**, 1295 (1978).
[33] P. T. Bonoli, R. L. Boivin, C. L. Fiore, *et al.*, Bull. Am. Phys. Soc. **46**, 54 (2001).
[34] M. A. Beer, S. C. Cowley, and G. W. Hammett, Phys. Plasmas **2**, 2687 (1995).
[35] R. L. Miller, F. L. Waelbroeck, A. B. Hassam, and R. E. Waltz, Phys. Plasmas **2**, 3676 (1995).
[36] R. J. Goldston, D. C. McCune, H. H. Towner, S. L. Davis, R. J. Hawryluk, and G. L. Schmidt, J. Comp. Phys. **43**, 61 (1981).
[37] G. Rewoldt, W. M. Tang, and R. J. Hastie, Phys. Fluids **30**, 807 (1987).
[38] L. R. Baylor, T. C. Jernigan, S. K. Combs, *et al.*, Phys. Plasmas **7**, 1878 (2000).
[39] G. Rewoldt and W. Tang, Phys. Fluids B **2**, 318 (1990).
[40] M. H. Redi, W. Dorland, R. Bell, *et al.*, 30th EPS Conf. on Contr. Fusion and Plasma Phys., St. Petersburg, 7-11 July 2003 ECA Vol. 27, P-3.98.
[41] J. E. Rice, P. T. Bonoli, C. L. Fiore, *et al.*, Nucl. Fusion **43**, 781 (2003).
[42] J. E. Rice *et al.*, Bull. Am. Phys. Soc. **48**, 18 (2003), Paper BI1.003, submitted to Phys. Plasmas (2003).
[43] S. P. Hirshman and D. J. Sigmar, Nucl. Fusion **21**, 1079 (1981).
[44] D. R. Ernst, M. G. Bell, R. E. Bell, *et al.*, Phys. Plasmas **5**, 665 (1998).
[45] B. B. Kadomstev and O. P. Pogutse, Sov. Phys.-JETP **24**, 1172 (1967).
[46] B. B. Kadomstev and O. P. Pogutse, Sov. Phys.-Dokl. **14**, 470 (1969).
[47] B. Kadomtsev and O. Pogutse, in *Reviews of Plasma Physics*, edited by M. Leontovich, Consultants Bureau, New York, 1970, volume 5, p. 249.
[48] J. C. Adam, W. M. Tang, and P. H. Rutherford, Phys. Fluids **19**, 561 (1976).
[49] C. Z. Cheng and L. Chen, Nucl. Fusion **21**, 403 (1981).
[50] B. Coppi and G. Rewoldt, Phys. Lett. A **49A**, 36 (1974).
[51] B. Coppi and G. Rewoldt, Phys. Rev. Lett. **33**, 1329 (1974).
[52] B. Coppi, S. Migliuolo, and Y.-K. Pu, Phys. Fluids B **2**, 2322 (1990).
[53] D. W. Ross, J. C. Adam, and W. M. Tang, Phys. Fluids **20**, 613 (1977).
[54] M. A. Beer, *Gyrofluid Models of Turbulent Transport in Tokamaks*, PhD thesis, Princeton Univ., Dept. of Astrophysical Sciences, 1995.
[55] S. Parker *et al.*, Bull. Am. Phys. Soc. **48**, 84 (2003), Paper FI1.005, submitted to Phys. Plasmas (2003).
[56] W. M. Tang, G. Rewoldt, and L. Chen, Phys. Fluids **29**, 3715 (1986).
[57] K. Hallatschek and W. Dorland, Bull. Am. Phys. Soc. **47**, 135 (2002), Paper GI1.005.
[58] M. N. Rosenbluth and F. L. Hinton, Phys. Rev. Lett. **80**, 724 (1998).
[59] B. N. Rogers, W. Dorland, and M. Kotschenreuther, Phys. Rev. Lett. **85**, 5336 (2000).
[60] M. Brambilla, Nucl. Fusion **38**, 1805 (1998).
[61] F. Jenko, W. Dorland, and G. W. Hammett, Phys. Plasmas **8**, 4096 (2001).
[62] E. J. Doyle, T. A. Casper, T. B. Kaiser, *et al.*, Bull. Am. Phys. Soc. **47**, 301 (2002).
[63] S. Ishida *et al.*, Bull. Am. Phys. Soc. **48**, 82 (2003), Paper FI1.2.